scientific reports

Check for updates

OPEN

A comprehensive analysis of the impacts of Image Resolution and Scanning Times on the quality of MPI-reconstructed images

Ton Duc Do[1,4]✉, Azamat Mukhatov[1,4], Aizhan Tolebay[3], Tuan-Anh Le[2] & Tri T. Pham[3]✉

Scanning trajectories are essential and important components of trajectory-based scanning and imaging systems such as laser scanning confocal microscopes, atomic force microscopes (AFM), laser scanning systems for aerial surveying (LiDAR), micro-electromechanical systems (MEMS), medical imaging and 2D/3D printing. Previous study has demonstrated that Sinusoidal Lissajous is the optimal scanning trajectory and proposed that increasing the scanning repetition could further enhance image quality. However, it is challenging to pinpoint the essential elements needed to enhance the quality of the reconstructed images since there is currently no comprehensive analysis of how the scanning trajectory resolution and scanning time affect the reconstructed image quality. The purpose of this work is to look into the influence of scanning resolution and scanning time on the quality of magnetic particle imaging (MPI)-reconstructed images across a variety of scanning trajectories. This study offers a comprehensive analysis of how scanning repetition and scanning time affect the reconstructed images' quality at the individual pixel in the field of view (FOV) as well as throughout the entire FOV. The impacts of the scanning time were investigated both before and after image reconstruction. In the pre-reconstruction phase, the minimum and maximum distances to the closest neighboring points in the FOV and their distribution in different regions of the FOV were analyzed in order to investigate the density, homogeneity, and time spent on each pixel. Here, we demonstrated that the image resolution for any scanning trajectory is scale invariance, meaning that for a fixed frequency ratio N_P, the ratio of pixel size to image FOV size remains constant. Peak signal-to-noise ratio (PSNR), structural similarity index measure (SSIM), normalized root mean square error (NRMSE), and normalized sum of squared error (NSSE) are used to evaluate and compare the reconstructed images' quality in the post-reconstruction stage. It is found that the Sinusoidal Lissajous scanning trajectory is the best in terms of accuracy, structural similarity, and signal-to-noise. We showed that only the image quality for bidirectional Cartesian and sinusoidal Lissajous trajectories are sensitive to scanning time, particularly at the pixel scale. Furthermore, contrary to expectations, we discovered that optimizing the scanning repetition did not enhance the MPI-reconstructed image quality. Nevertheless, the image quality would be enhanced by extending the scanning duration through decreasing the scanning frequency. The optimal scanning frequency is half of the frequently used 25 kHz for the chosen N_P ratio of 100.

Keywords Scanning trajectory resolution, Scanning repetition, Scanning time, Scale invariance, Optimal scanning frequency

Nowadays, scanning methods are an essential part of many of the applications we use on a regular basis. Scanning trajectories are applied in a variety of industries, including medical imaging[1,2], industrial quality control[3], security and surveillance[4], geographic information systems (GIS)[5], archaeology and cultural heritage preservation[6], robotics and automation[7], digitalization and document management[8], reverse engineering and

[1]Department of Robotics, School of Engineering and Digital Sciences (SEDS), Nazarbayev University, Astana 010000, Kazakhstan. [2]Department of Physiology and Biomedical Engineering, Mayo Clinic, Scottsdale, AZ 85259, USA. [3]Department of Biology, School of Sciences, Humanities Nazarbayev University, Astana 010000, Kazakhstan. [4]Ton Duc Do and Azamat Mukhatov have equal contributions. ✉email: doduc.ton@nu.edu.kz; tri.pham@nu.edu.kz

prototyping[9], forensics and crime scene investigation[10], robotics and virtual reality[11]. Medical or biomedical imaging, however, is one of the most significant domains where scanning trajectory is employed.

Medical imaging, which includes newer modalities like magnetic particle imaging (MPI), is fundamental to contemporary healthcare and propels advancements in research, diagnosis, treatment, and personalized medicine[12]. MPI holds significant potential for in vivo cell tracking[13], high-contrast angiograms[14], cancer imaging[15], and imaging of inflammation in both small animal and human subjects[15,16].

MPI offers the ability to quantify the amount of saturated superparamagnetic nanomaterials in the field of view (FOV) of interest[17]. Although MPI cannot directly visualize the tissue or organ, it can detect the magnetic nanoparticles injected in the body to target specific body part of interest such as cancer tumors[18]. Magnetic nanoparticles (MNPs) are minuscule particles in the nanometer size range that are magnetized. An MPI scanner is constructed by positioning two powerful magnets (selection coils) facing each other in Maxwell configuration to make a center-based field free point (FFP) magnetic field. Other coils, known as driving coils, create an alternating magnetic field at kHz frequencies. This field is not only used to scan the FFP within an drive-based FOV (D-FOV) for imaging, but also to oscillate particle magnetization and generate particle signals that can be measured by other specific coils, known as receiver coils[19]. Nonlinearities, such as the extremes of a magnet's strength, are the building blocks of harmonics, and the strength of these structures is proportional to the particle count. Signal detection and spatial information encoding are aided by the static gradient field, generated by the selection coils. MNPs within the FFP can follow the magnetic field; but, outside of the FFP, the MNPs have been saturated by the strong static field., making it impossible to distinguish the signal[20].

Since the amplitude of the drive fields has limitation because there is a chance of unpleasant peripheral nerve stimulation (PNS), the D-FOV only can cover a small FOV such as animal scale. To cover a larger FOV for human-scale, time-varying focus fields with much lower frequency (< 100 Hz) need to be used to steer D-FOV to cover all area of the FOV. MPI can swiftly generate 3D images of the complete heart or brain in second[21]. The magnetization of the MNPs and the magnetic gradient's strength in the D-FOV/FOV determine the sensitivity and accuracy of MPI image detection. The MPI scanners currently available on the market for animal scale have a range of one to several millimeters of spatial resolution[22,23].

Nonetheless, the efficient functioning of the MPI system depends on optimizing scanning trajectories, both in terms of hardware control and the quality of the reconstructed images. Examining these trajectories is crucial for improving spatial resolution, decreasing artifacts, and boosting acquisition efficiency in MPI systems. By improving the quality of the reconstructed images and reducing scan times, researchers can eventually boost MPI's efficacy in medical imaging. The selection of a suitable scanning trajectory depends on several elements, such as covering area, speed, accuracy, and resolution[12,24]. Furthermore, the objective of the application, nature of recorded data, and scanning technologies have a considerable influence on the type of chosen trajectory[25].

Several criteria are necessary to ensure high-quality results in the field of scanning systems, especially in imaging applications like microscopy or biomedical imaging. Among these, timing, proper scanning trajectory selection, resolution selection, and accurate resolution calculation independent of the FOV geometry are critical. These elements are essential to take into account during system design and operation since they each significantly affect the quality, accuracy, and efficiency of the scanning process.

It is equally vital to choose the right scanning trajectory since it determines how the scanning density is distributed across the FOV[26,27]. Different scanning paths, such as radial Lissajous (RL), sinusoidal Lissajous (SL), triangular Lissajous (TL), and bidirectional Cartesian (BC), each offer unique benefits and drawbacks (refer to Table 1; Fig. 1(a) for more details). For instance, BC scanning is straightforward but may lead to oversampling or under sampling in certain areas, while some Lissajous patterns provide more even coverage but might be more challenging to implement. Therefore, before selecting the optimal trajectory for a given application, it is crucial to understand several trajectories and assess how they impact pixel distribution, coverage efficiency, and image quality. Uneven pixel distribution, duplicate data, or incomplete scan could result from poor trajectory selection, all of which may affect image quality[28].

The regularity of the scanning pattern and its density or scanning resolution are the primary determinants of the reconstructed image's quality. The two main categories of resolution to take into account are image resolution

Trajectories	Mathematical Expression	Frequency Ratio	Repetition Time
Bidirectional Cartesian	$H_x(t) = \{Asin(2\pi f_x t),\ t < \frac{T_R}{2}\ Bsin(2\pi f_y t + \varphi),\ t \geq \frac{T_R}{2}\}$ $H_y(t) = \{Asin(2\pi f_y t + \varphi),\ t < \frac{T_R}{2}\ Bsin(2\pi f_x t),\ t \geq \frac{T_R}{2}\}$	$f_y = \frac{2f_x}{N_P}$	$T_R = \frac{N_P}{f_x}$
Triangular Lissajous	$i_x = Asawtooth(2\pi f_x t)$ $i_y = Bsawtooth\left(2\pi f_y t + \varphi\right)$	$f_x = \frac{N_P}{N_P - 1} f_y$	$T_R = \frac{N_P}{2f_x}$
Sinusoidal Lissajous	$i_x = Asin(2\pi f_x t)$ $i_y = Bsin\left(2\pi f_y t + \varphi\right)$	$f_x = \frac{N_P}{N_P - 1} f_y$	$T_R = \frac{N_P}{f_x}$
Radial Lissajous	$i_x = Asin(2\pi f_x t) * sin(2\pi f_y t)$ $i_y = Bsin(2\pi f_y t) * cos(2\pi f_x t)$	$f_x = \frac{N_P}{N_P - 1} f_y$	$T_R = \frac{N_P}{f_x}$
Here, f_x is the fundamental frequency in x-direction, f_y is the frequency in y-direction, N_P is the integer coefficient, T_R is repetition time, φ is the phase, A, B are the amplitudes, t is time[29].			

Table 1. Mathematical expressions for all scanning trajectories used in this work29.

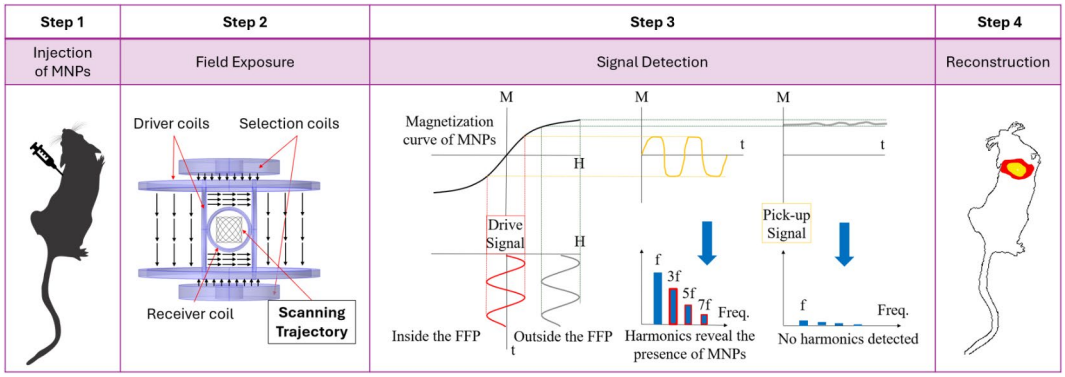

Fig. 1. Overview of Magnetic Particle Imaging (MPI) process

and spatial resolution. Spatial resolution is the smallest observable detail that the imaging system can detect. The resolution, or amount of detail, of an image is determined by its total number of pixels. The resolution of an image is based on the size and quantity of its pixels, which are its smallest unit. A fixed-size image with many little pixels, for instance, will have a greater resolution since it can display more detail. Less detail and perhaps a pixelated appearance result from reduced resolution caused by fewer large pixels. Resolution and pixel size are therefore inversely correlated; as pixel size decreases, resolution increases, and vice versa. High-resolution images are distinguished by sharper details and better clarity since they can capture subtle aspects inside an image. The resolution to be used depends on the specific needs of the application. A better image resolution with smaller pixel sizes is required for tiny details, such as imaging at the cellular and subcellular levels. However, in other situations, a lower resolution may be sufficient, reducing processing time and the amount of data that needs to be processed and stored. Selecting the appropriate resolution ensures that the picture retains all the necessary information without investing excessive amounts of data and time[29,30].

Estimating the resolution and how it affects image quality across various FOV types - such as rectangular, square, circular, or elliptical - is one of the trickiest parts of scanning. The size and shape of the FOV may have an impact on the pixel size and scanning pattern, making it more challenging to determine the ideal resolution. It is essential to have a reliable resolution estimation method that is applicable to every FOV shape since it ensures constant image quality under all scanning conditions. This is particularly important when using a single scanning device for multiple applications with varying FOV geometries. In addition to allowing operators to predict crucial scanning parameters like trajectory and time, accurate resolution prediction ensures consistent image quality across various FOV configurations. All of these aforementioned elements are interrelated and understanding how each of the components affects the reconstructed image's quality ensures that the system can produce high-quality images fast and reliably in fields where precision and reliability are essential.

Therefore, this study focuses on evaluating the impact of image resolution and scanning time on the reconstructed images' quality for various trajectories used in biomedical imaging, including BC, TL, SL, and RL. The following section will show how to calculate the maximum pixel size for all scanning trajectories with varied parameters. Then the link between pixel size, FOV size, and shape will be determined. The quality of image reconstruction for each trajectory will be assessed and compared. Furthermore, the impact of scanning repetition and scan time on reconstructed image quality will be explored. The investigation will also look at how much time is spent on each pixel and how it affects image quality.

Methods

A state-of-the-art imaging technique for highly sensitive and high-resolution visualization of magnetic nanoparticles (MNPs), Magnetic Particle Imaging (MPI) is summed up in Fig. 1. In the first step of the procedure, magnetic nanoparticles (MNPs) are injected into the subject. These particles accumulate in the target area due to specific biological mechanisms or targeting methods. Step 2 involves exposing the subject to magnetic fields produced by the MPI apparatus. Drive coils dynamically shift the FFP along a predetermined scanning trajectory to cover the imaging volume, whereas selection coils produce a high-gradient magnetic field with a field-free point (FFP). Step 3 is signal detection, in which the magnetization response of the MNPs is recorded by receiver coils. Within the FFP, the MNPs' non-linear response produces harmonics; outside of it, no harmonics are produced. The particles are spatially localized by processing this signal. Lastly, Step 4 creates an image that maps the distribution of MNPs in the target area by reconstructing the detected data. This method makes MPI a cutting-edge tool for biomedical applications like disease detection, drug delivery monitoring, and vascular imaging by enabling real-time, non-invasive imaging with high contrast and specificity.

Understanding the critical factors that govern the trajectory's performance is necessary to compare how well different scanning trajectories perform in terms of the scanning pattern's density and the quality of the reconstructed images[27,31].

First, we identify and use the crossing points where two scan lines overlap as reference points; these are the blue dots in Fig. 2 (a). Here, one can see that for each crossing point away from the boundary, there are six nearest neighbor points, and D_{min} and D_{max} are the minimum and maximum distance to these points (see Fig. 2 (b) for a zoomed-in version of all trajectories).

The distances to the six nearest neighbors of each crossing point in the FOV are calculated and sorted to get the D_{min} (red dash line) and D_{max} (green dash line) values. The pixel size of the scanning pattern should be set using the maximum of all the minimum values because each crossing point has its own D_{min} and D_{max} values. In general, each crossing point has eight nearest neighbors, but the last two farthest nearest neighbor points are not required to calculate the image resolution. This is because the shortest distance between the two parallel nearest neighbor lines will always be used to calculate the pixel size and hence the image resolution.

Although D_{min} and D_{max} are the straightforward definitions of distance that almost equals the pixel size, they don't exactly represent the true pixel size of the scan pattern. In reality, a more precise representation is often used to calculate the pixel size which is the longest perpendicular distance between 2 adjacent scan lines in the FOV as shown by H_{max} in Fig. 2 (b). To calculate H_{max} at each crossing point, the longest perpendicular distance from the focus/center crossing point to all the nearest adjacent scan lines is calculated. D_{min} and D_{max} are required to calculate H_{max}. Two to four values of H_{max} were acquired depending on the irregularity of the scanning trajectory and they were sorted to get the maximum value. In other words, the values of H_{max} depend on the scanning trajectory and can be four distinct values or two pairs of values.

The maximum value of H_{max}, $D_{min,}$ and D_{max} for all points in the FOV are stored because these values are closer to the pixel size, especially the H_{max}. This way of estimating the pixel size will prevent underestimation or overestimation of the image resolution if the average of all the calculated distances in the FOV is used.

Adopting the strategy from previous work[32], various distances between the center overlapping focus point to the nearest neighboring overlapping points (H_{max} is the distance from a focus point to the closest orthogonal scanning line, D_{min} is the distance from a focus point to closest neighbor point, D_{max} is distance from a focus point to furthest neighbor point and $D_V$is the Voronoi distance or the distance from a focus point to the further edge vertex of a Voronoi cell surround the focus point[30,32]) are evaluated and compared across four different trajectories as shown in Fig. 2(a)-(b) and Table 2. In addition, the Voronoi distance (D_V)is also evaluated for comparison with the three previously defined distances. Some articles consider the Voronoi distance as standardized measurement for different scanning trajectory comparison[29,32–34]. By reducing the Voronoi distance and equalizing it on whole FOV, the scanning trajectory can be assumed good for image reconstruction. It is important to note that Voronoi distance is merely an estimate and does not correspond to any actual distance seen in the scanning pattern. Figure 2(b) demonstrated the definition of all of these distances for all four different scanning trajectories at the integer coefficient N_P, which defines ratio between frequencies in x and y directions[32]. $N_P = 100$was chosen based on the previous works, which proved that this value is sufficient to obtain a high spatial resolution scan, to produce a good quality image, and minimize aliasing in the images[33]. Moreover, $N_P$values from 10 to 400 were also tested previously, and similar conclusion was made[32]. Furthermore, choosing this value is a practical compromise between resolution and hardware/computational load.

For this work, the parameters setting from previous studies were used where the frequency for $f_x$was set at 25 kHz, the width and length of the FOV were set at 3.2 cm and 1.6 cm, respectively[32,33,35].

The phantom images were built using the image resolution of the suggested scanning trajectories[36]. Since MPI is one of the key applications for the previously mentioned scanning techniques, MPI image reconstruction will be used to perform further analysis. System matrix was chosen as an image reconstruction method because of its high accuracy[29]. This method is superior to previous strategies because any kind of trajectory can use it. The phantom images were generated with the assumption that the white part inside the image were filled with super-paramagnetic iron oxide nanoparticles (SPIONs) as shown in Fig. 4.

Table 2 depicts the parameters setting required for the MPI image reconstruction. In general, H_{max} was used to define the pixel size. The width and height of each phantom were divided by half of $H_{max}$to obtain the quantity of pixels on each phantom side length[30,32].

Here, value of $H_{max}$for the BC trajectory was used to build the phantom image because it has the highest pixel size across all four selected trajectories. This choice of pixel size will ensure that all scanning trajectories will have sufficiently high fill factor to achieve the best image quality as demonstrated in previous work[32]. Different conditions were used to simulate the reconstructed image such as variation in the scanning cycle or repeat: 1 repeat (1R), 2 repeats (2R), 4 repeats (4R) and 8 repeats (8R) as well as changing the scanning time by reducing the fundamental frequency (f_x) to half (HF), quarter (QF) and half of a quarter (HQF) (see Fig. 4 for more details).

To assess the quality of reconstructed images, it is essential to measure the similarity and difference of the constructed image with the phantom to assess the accuracy of the method. Although there is some definitional overlap among PSNR, NRMSE, NSSE, and SSIM, each metric provides a unique perspective on the image's quality, therefore all are required for a thorough assessment. The ratio of signal power to noise power is used

Diameter of Particle	30.10^{-9}m
Temperature	310 K
Air Permeability	$4x.10^{-7}N/A^2$
Particles Concentration	1.5 mol/m^3
Molar Mass of Magnetite	0.231 kg/mol
Density of Magnetite	5170 kg/m^3
Magnetization of Magnetite	$4.77.10^5$A/m

Table 2. Parameters for image reconstruction.

by PSNR to assess perceptual similarity, while NRMSE provides a scale-independent measure of reconstruction accuracy that allows comparisons between images with varying intensity ranges. In addition, NSSE examines the total error between the ground truth and the reconstructed image. Perceptual variations in brightness, contrast, and structural content are examined using SSIM in order to determine structural similarity. When taken together, these measurements provide strong validation of our assertions across various aspects of image quality, allowing us to be more confident in the results.

Peak signal-to-noise ratio (PSNR) is used to determine how closely the reconstructed image resembles the phantom one[37]:

$$PSNR = 10log_{10}\left(\frac{1}{n}\sum_{i=1}^{n}(x_r - x_p)^2\right)^{-1} \tag{1}$$

In this case, x_p symbolizes the phantom's intensity., whereas x_r is the intensity of the reconstructed image.

Structural Similarity Index Measure (SSIM) is another metric to evaluate the accuracy of the reconstruction. When comparing two images, it is used to gauge how similar they are and is defined as:

$$SSIM = \frac{(2\bar{x}\bar{y} + c_1)(2\sigma_{xy} + c_2)}{(\bar{x}^2 + \bar{y}^2 + c_1)(\sigma_x^2 + \sigma_y^2 + c_2)} \tag{2}$$

here $\bar{x}$ and $\bar{y}$ represent the mean over a window in Image *X* and Image *Y*, respectively. σ_x and σ_y are the standard deviations over a window in Image *X* and Image *Y*. σ_{xy} is the co-variance over a window between Image *X* and Image *Y*, c_1 and c_2 are constants.

In addition to peak signal-to-noise and structural similarity, the normalized root mean square error (NRMSE) was also used quantify the precision of the reconstructed image. NRMSE is determined via the following formula:

$$NRMSE = \sqrt{\frac{\sum_{i=1}^{n}(x_r - x_p)^2}{\sum_{i=1}^{n}(x_p)^2}} \tag{3}$$

Normalized sum of squared errors (NSSE) is another metric to measure the accuracy of the reconstructed images and it is defined as follows:

$$NSSE = \frac{\sum_{i=1}^{n}(x_r - x_p)^2}{\sum_{i=1}^{n}(x_p)^2} \tag{4}$$

The values of PSNR, SSIM, NRMSE and NSSE will be showed and analyzed in next section.

Results and discussion

Scanning patterns and characteristics

Table 3 displayed the estimated values for the distance H_{max}, D_{min}, D_{max} and D_V obtained from four different types of trajectories referred in Fig. 2(a)-(b). These values are obtained from scanning trajectories with $N_P = 100$[29]. The data clearly showed that the RL trajectory had the lowest values at all distances, as observed in our earlier work[30]. This is followed by the SL, TL, and BC trajectories. It should be emphasized that for estimation of image resolution, values of H_{max}were used since they accurately and precisely indicate the resolution in comparison to the remaining distance metric[30,38].

Figure 2(c)-(d) illustrate the definition of the distances and their distribution or the heat map in the FOV for different scanning trajectories. According to Fig. 2(c)-(d), TL is the most regular or uniform trajectory. The largest gaps are found in BC, indicating that scanning will be less precise or lower resolution, and some areas may be missed. SL has larger gap in the center and increasing density toward to borders. For RL, middle and edges are densest, but the FOV is not fully covered, resulting in an ellipsoid shape rather than a rectangle. Figure 2(e) shows how much time the scanner spent on each pixel. For BC and SL, the scanner spent more time at the boundary than in the center of the FOV. For the TL, time is equally distributed across all pixels, whereas for the RL, the scanner spends the majority of its time at the center and the boundary region.

	Max H_{max}	Max D_{min}	Max D_{max}	Max D_V
BC	0.502	0.502	0.503	0.551
TL	0.287	0.320	0.361	0.402
SL	0.225	0.251	0.283	0.316
RL	0.166	0.188	0.195	0.255

Table 3. Maximum distance (in mm) from a focus point to neighboring points in the FOV for different trajectories with N_P=100.

Scale invariance of the Image Resolution

It is essential to quantify the regularity of the scanning pattern and their distribution in the FOV. To do so, the ratio of the minimum distances to their maximum counterparts in a selected FOV region are analyzed. Figure 3(a) shows the changes in this ratio as the region of the FOV is increasing, which is expressed in terms of the fractional length of the FOV. The red boxes are the areas that satisfy the percentage of the width or length of the FOV. Figure 3(b) illustrates the ratio of $\frac{Min\ D_{min}}{Max\ D_{min}}$ and $\frac{Min\ D_{max}}{Max\ D_{max}}$ for different trajectories at $N_P = 100$. It is very clear that these ratios for TL are constant and close to unity because the TL generates a very regular and uniform pattern. The ratio for SL is decreasing as fractional length increases from the center of the FOV, indicating that SL has denser pattern near the boundaries compared to middle. BC has small values of $\frac{Min\ D_{min}}{Max\ D_{min}}$ because of dense D_{min} behavior. However, D_{max} decreases near borders as shown on Fig. 3(b). The ratios for RL are almost zeroes because it has dense structure in both D_{min} and D_{max} cases.

In previous work, we have shown that relationship between H_{max} and $N_P$is as follows[32]:

$$H_{max} = \frac{b}{N_P} \tag{5}$$

where b is the constant and N_P is integer coefficient, which is used to define the ratio between the two driving frequencies in the x and the y directions.

In order to explore the influence of the choice of FOV on the value of H_{max}, the above formula can be transformed into the following formula by dividing both side with an effective length of the FOV used. The result is the following formula:

$$\frac{H_{max}}{L_{EFF}} = \frac{c}{N_P} \tag{6}$$

where c is a constant and L_{EFF} is the effective length of the FOV, which is defined as:

$$L_{EFF} = \frac{XY}{\sqrt{X^2 + Y^2}} \tag{7}$$

where X and Y are length and width of the scanning FOV.

Figure 3(c)-(d) show the values of $\frac{H_{max}}{L_{EFF}}$ for a wide range of N_P values ranging from 10 to 400 for both rectangular and square FOV at various side lengths. The results clearly show that the size of the FOV does not have an influence on this ratio for any scanning trajectory with a fixed N_P value. This indicate that the ratio of $\frac{H_{max}}{L_{EFF}}$ is scale invariance and is independent of the size of the FOV.

The field of view geometry has a big impact on scanning trajectories and image resolution. A square FOV with equal dimensions is uniform and isotropic because it is symmetrical. A rectangular FOV with varying widths and heights makes designing scanning trajectories more difficult, particularly in terms of frequency selection for

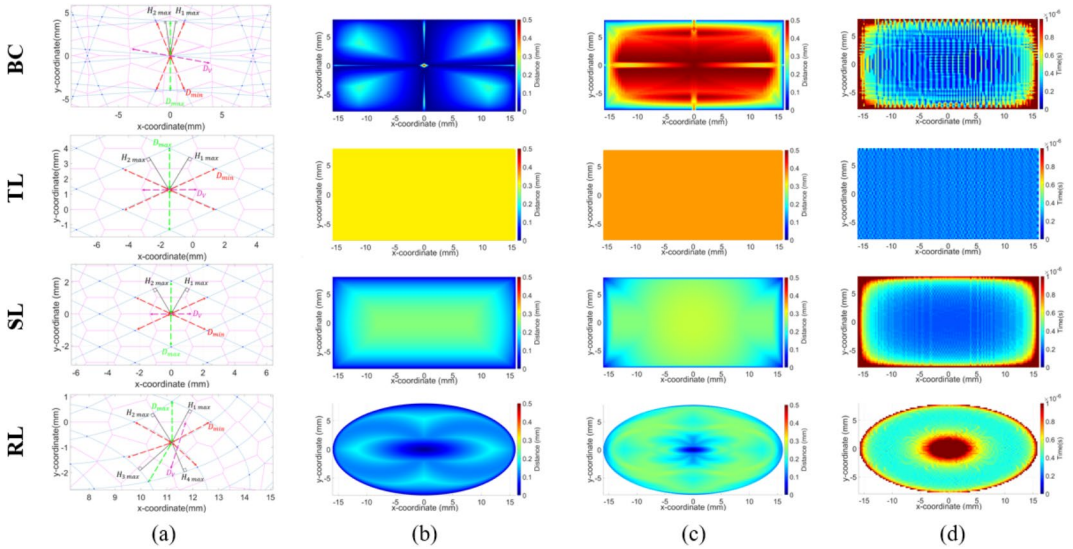

Fig. 2. (a) Patterns of all four scanning trajectories for N_P=12 (b) Representative zoomed in image of region in the FOV where the distances D_{min}, D_{max} and H_{max} are largest. (c) Heat map displaying the distribution of minimum distance D_{min} in the FOV, (d) heat map for the distribution of maximum distance D_{max}, and (e) heat map for the total time spent on each individual pixel for N_P=100 using the image resolution of the BC mesh.

the x and y directions, which might affect image resolution. Aspect ratio differences in rectangular FOVs might result in non-uniform pixel sizes and anisotropic resolution if not handled appropriately. This understanding can lead to a better selection of scanning parameters to enhance scanning resolution.

Quality of Image reconstruction

The discrepancy between the phantom's and the reconstructed image's sizes presented a major barrier for Magnetic Particle Imaging (MPI) reconstruction at first. This disparity rendered the comparison between the real phantom and its reconstruction untrustworthy since the size variations resulted in inaccurate assessments of the reconstruction's quality. Early on, the reconstructed image was frequently either bigger or smaller than the phantom, which led to ambiguity in the experimental results and distorted metrics for performance evaluation. In the present work, the reconstructed image was generated utilizing interpolation and cropping techniques to exactly match the phantom image's actual physical dimensions. This phase was essential for removing discrepancies and improving the comparison's accuracy. These techniques also allowed us to avoid the "Inverse Crime" issue by ensuring that the pixel size of the phantom image should always be smaller than the pixel size of the reconstructed image. We were able to avoid pitfalls by carefully scaling the reconstruction, which made it possible to evaluate the image reconstruction quality more realistically. The MPI technique's dependability was greatly increased by this increase in picture size uniformity, yielding more precise and reproducible results.

To compare the quality of MPI reconstructed images, NU and vascular phantoms were used in this work as shown in Fig. 4. Three different scanning repeats (2R, 4R and 8R) and three different scanning times (HF, QF and HQF) were selected to evaluate and compare with the standard 1R scan. Table 4 shows the values of PSNR, SSIM, NRMSE and NSSE for both phantom images for all four scanning trajectories at standard scanning time as well as doubling the scanning time. While RL has the highest resolution among all four trajectories, its performance on the image reconstruction is terrible and the NRMSE and NSSE values are much higher than the other trajectories. In addition, RL does not cover corners of the FOV, thus it cannot be chosen as optimal one. BC trajectory is the next up on the performance list, but it is not better than TL and SL trajectories. SL and TL are the best performers. TL slightly outperformed SL when using standard one repeat (1R) scan. However, SL performed better than TL when increasing the scanning time to double of the standard 1R scan.

Figure 5(a)-(d) demonstrate the influence of scanning repetition and scanning time on the quality of reconstructed image for all four trajectories using two different phantom images. To exclude the influence of the background noise on the accuracy of the measuring metrics, comparison of only the phantom region (i.e. the white part in the phantom image) was also conducted. Here, Fig. 5(a) and (c) present the analysis of the entire image while Fig. 5(b) and (d) represent the results for only the phantom with the background being removed. The difference between phantom-only and full images is often that the error is lower when comparing phantom-only images, indicating that removing the background noise improve the accuracy of the comparison. The results unambiguously demonstrate that RL performs poorly on every metric. In general, the reconstructed image's quality is not enhanced by increasing the scanning repeat for all trajectories. Furthermore, extending the scan

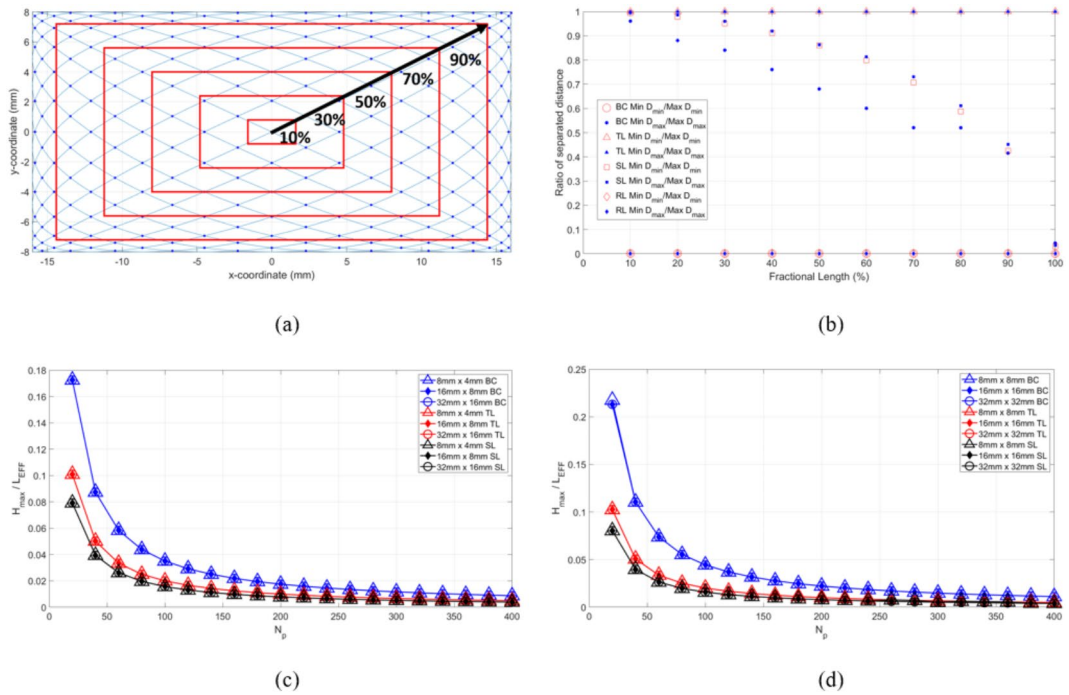

Fig. 3. (a) Region of defined fractional length in the FOV. (b) Ratio between D_{min} and D_{max} for BC, TL, SL and RL trajectories at N_P=100. (c) Ratio between H_{max} and effective length FOV_{xy} for rectangular FOV and (d) for square FOV for different scanning trajectories at various N_P values.

		1R				HF			
Type	**Trajectory**	**PSNR**	**SSIM**	**NRMSE**	**NSSE**	**PSNR**	**SSIM**	**NRMSE**	**NSSE**
NU	BC	18.707	0.755	0.319	0.102	19.800	0.831	0.282	0.079
	TL	19.949	0.814	0.277	0.077	19.965	0.844	0.276	0.076
	SL	19.470	0.622	0.293	0.086	20.418	0.715	0.262	0.069
	RL	17.979	0.623	0.347	0.121	18.652	0.629	0.321	0.103
Vascular	BC	20.218	0.832	0.401	0.161	21.809	0.912	0.334	0.112
	TL	21.212	0.859	0.358	0.128	21.633	0.912	0.341	0.116
	SL	21.100	0.703	0.363	0.131	22.159	0.847	0.321	0.103
	RL	21.000	0.877	0.367	0.134	21.144	0.818	0.361	0.130

Table 4. Comparison of the reconstructed image quality for all trajectories using the BC mesh with the standard 1 repeat (1R) and doubling the scanning time or half frequency (HF).

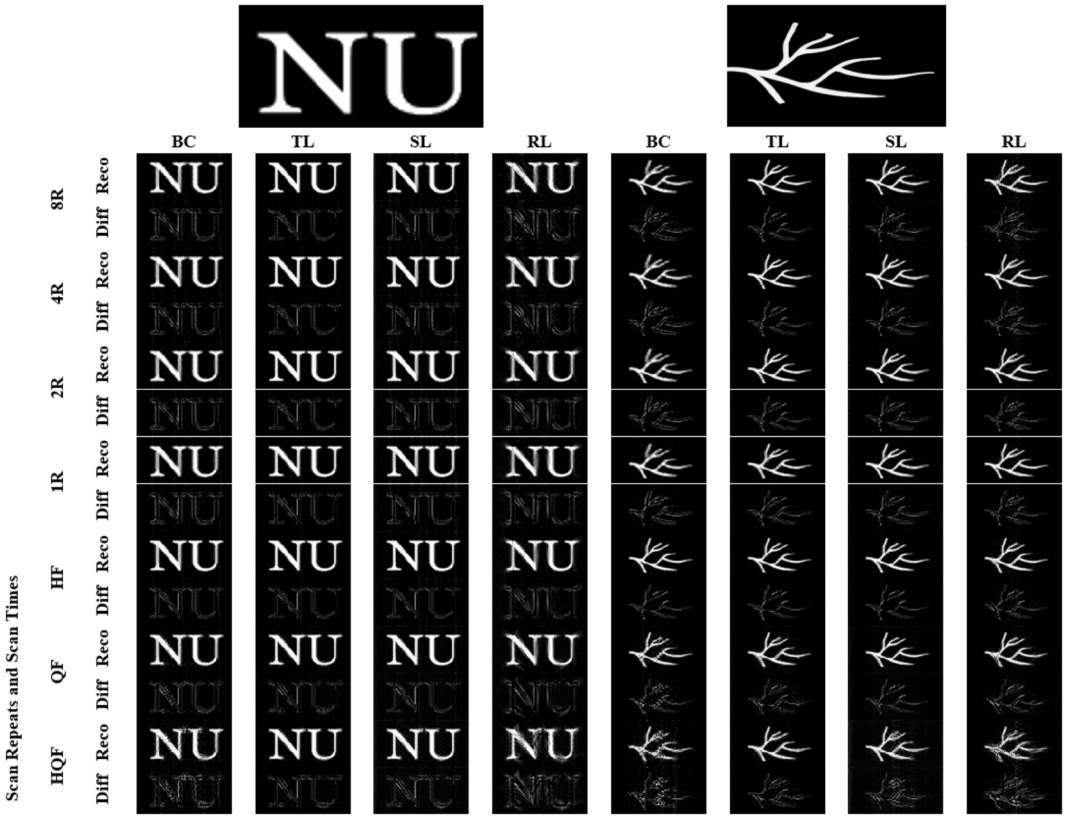

Fig. 4. Reconstructed images of NU and Vascular phantoms N_P=100 BC mesh for different scanning techniques and various cases such as 8 repeats (8R), 4 repeats (4R), 2 repeats (2R), 1 repeat (1R), Half Frequency (HF), Quarter Frequency (QF) and Half Quarter Frequency (HQF).

duration or cutting the frequency in half have no beneficial effects on the TL trajectory. However, doubling the scan time improves the reconstructed images' quality for both BC and TL trajectories. Increasing the scan time to QF or HQF further does not improve the results. The ideal scanning duration for the configuration employed in this work is therefore half of the chosen frequency of 25 kHz. Thus, the SL at half frequency produces the best reconstructed image quality.

Effects of scanning time on each pixel

To comprehend how scan time affects the quality of reconstructed images, the correlation between image quality and the time spent on each individual pixel in the FOV was also investigated. The intensity difference for each pixel in the reconstructed images is determined by directly comparing them to the ground truth phantom images. The intensity difference is the absolute difference between each pixel's intensity value in the reconstructed image and its corresponding pixel's intensity value in the phantom image. After that, these variations are displayed to illustrate the spatial distribution of errors within the FOV. The time spent on a pixel by the scanner is divided

into three different categories: the minimum continuous time spent, the maximum continuous time spent, and the total time spent. Figures 6 and 7 show the effects on pixel scanning time or dwell time on the quality of reconstructed image. Figures 6 and 7 (b), (f), and (j) show that increasing the time spent on each pixel in TL scan does not reduce the difference or the error level, indicating that the error is not dependent on time. This also verifies that TL follows a uniform pattern and spends the same amount of time on pixels across the FOV. Figures 6 and 7(d), (h), and (l) illustrate that RL has a large number of errors despite increasing the time spent on each pixel. Figures 6 and 7(a), (e), and (i) show that BC has a high degree of errors and resembles RL. Nevertheless, as scan time increases, the errors for this trajectory decrease[39]. The optimal trajectory, SL, of all the choices clearly shows a low degree of error or deviation, which improves as scanning duration increases (see Figs. 6 and 7 (c), (g), (k)). This explains why slowing down the SL scan improves the reconstructed images' quality as observed in Fig. 5.

Although SL is the best scanning trajectory in many ways, it is unable to produce a uniform pattern like the TL trajectory. This has considerable drawbacks, including uneven signal-to-noise, non-uniform resolution, and uneven error distribution across the field of view. Thus, it is critical to establish a balance between the regularity and density of the scan trajectory to enhance accuracy while preserving an even distribution of the aforementioned features. Future studies will focus on designing new scanning trajectories that can yield more uniform patterns while retaining image resolution and achieving acceptable image reconstruction quality. The results in this research provide a foundation for applications in various scanning technologies, including LiDAR and MEMS, as well as for improvements in MPI. These findings provide a means to improve performance in a variety of domains that need precise tracking and mapping, such as micro-electromechanical systems and autonomous car navigation, by improving scanning trajectories and spatial mapping methods. The wider applicability of these findings highlights their potential for widespread gains in scanning accuracy and efficiency and creates new opportunities for trajectory and image accuracy optimization across several technological platforms.

Conclusion

This paper aims to investigate the impacts of scanning repetition and scanning time on the quality of MPI reconstructed images for various scanning trajectories. Comprehensive assessments of scanning trajectories that could be used as a foundation for future studies in this field are currently lacking. Both before and after the reconstruction, the trajectory behavior and timing are studied. The research is separated into two parts: scanning pattern and image reconstruction analysis. The scanning pattern segment investigated the distribution of density in the FOV, followed by the effects of FOV size on scanning resolution for both rectangular and square-shaped images. It was discovered that the ratio of pixel size to FOV size is scale invariant, implying that this scaling can be applied to any FOV size of interest provide that the N_P value is the same. In the image reconstruction analysis, peak signal-to-noise, structural similarity and accuracy were used as the metric to compare the image

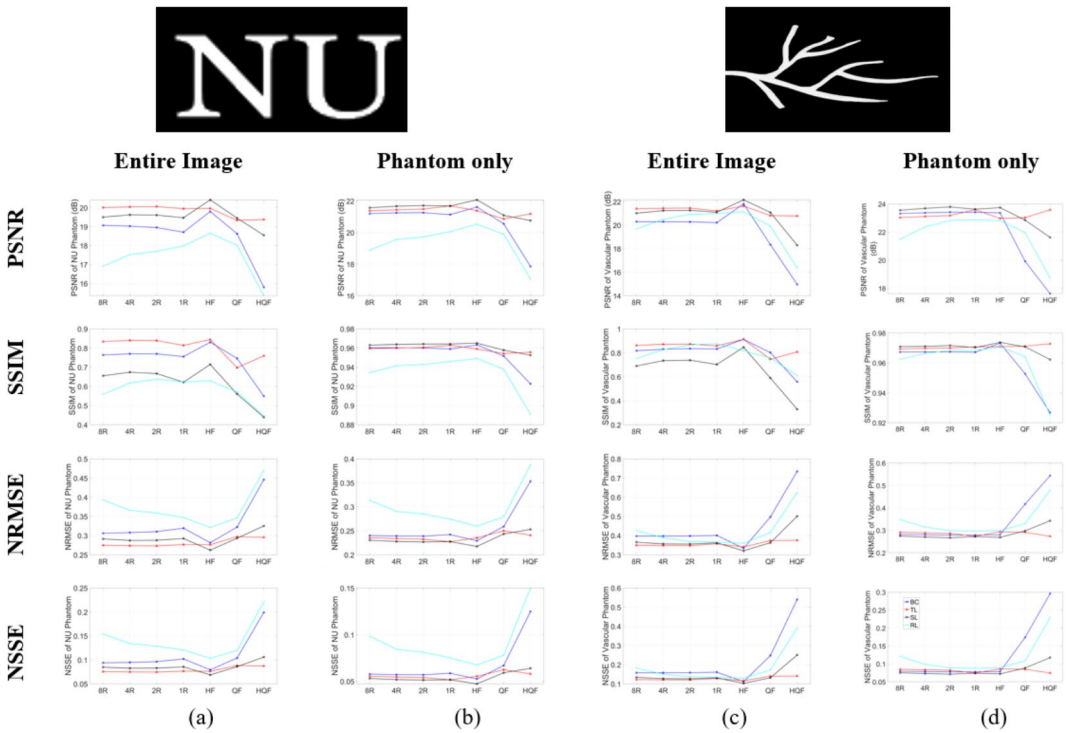

Fig. 5. Analysis of (a) NU phantom entire image, (b) NU phantom only (c) Vascular phantom entire image (d) Vascular phantom only calculated over different cases such as 8R, 4R, 2R, 1R, HF, QF, and HQF of scanning for various methods with N_P=100 at BC mesh.

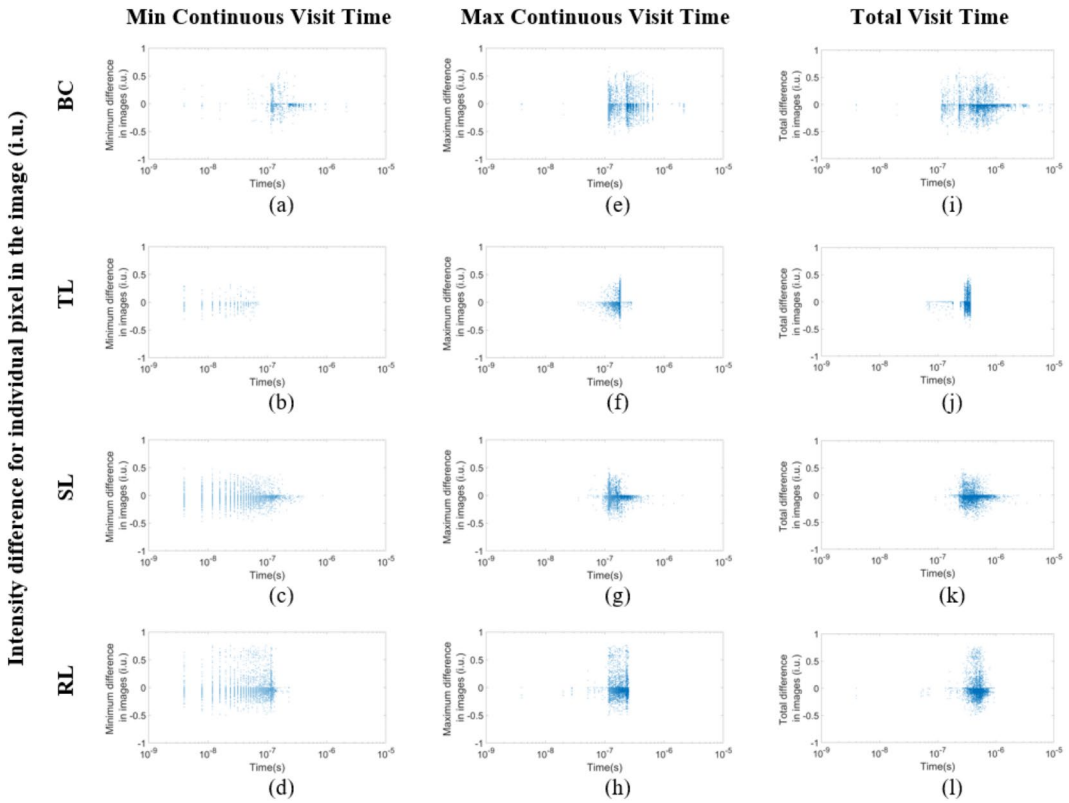

Fig. 6. Difference in intensity between the reconstructed image and the phantom of NU image for a)-d) for the minimum continuous time spent on a pixel, e)-h) for the maximum continuous time spent on a pixel)-l) total time spent on a pixel for various trajectories at N_P=100 using the BC mesh.

quality. It was determined that raising the scanning frequency did not increase image quality. However, doubling the scanning time can dramatically minimize errors and increase the reconstructed image's quality, particularly for the BC and SL trajectories. The ideal choice for the parameters utilized in this work is an SL trajectory with a frequency halved from the commonly used 25 kHz frequency.

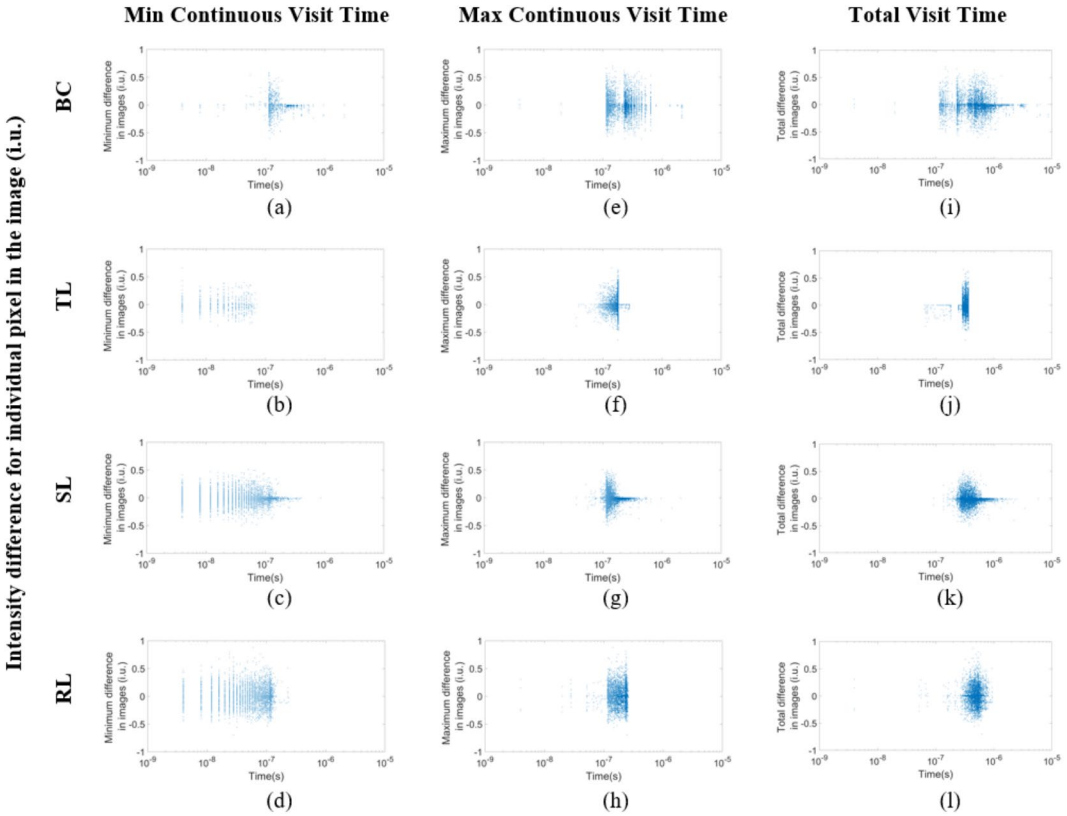

Fig. 7. Difference in intensity between the reconstructed image and the phantom of Vascular image for a)-d) for the minimum continuous time spent on a pixel, e)-h) for the maximum continuous time spent on a pixel)-l) total time spent on a pixel for various trajectories at N_P=100 using the BC mesh.

Data availability

The datasets used and/or analysed during the current study available from the corresponding author on reasonable request.

Received: 23 November 2024; Accepted: 4 February 2025
Published online: 14 February 2025

References

1. Kasban, H., El-Bendary, M. A. M. & Salama, D. H. A comparative study of medical imaging techniques. *Int. J. Inform. Sci. Intell. Syst.* **4**, 37–58 (2015).
2. Mukhatov, A., Le, T. A., Pham, T. T. & Do, T. D. A comprehensive review on magnetic imaging techniques for biomedical applications. *Nano Select*. **4**, 213–230 (2023).
3. Honarvar, F. & Varvani-Farahani, A. A review of ultrasonic testing applications in additive manufacturing: defect evaluation, material characterization, and process control. *Ultrasonics* **108**, 106227 (2020).
4. Bauweraerts, P. & Meyers, J. Reconstruction of turbulent flow fields from lidar measurements using large-eddy simulation. *J. Fluid Mech.* **906**, A17 (2021).
5. Borcs, A. & Benedek, C. Extraction of vehicle groups in Airborne Lidar Point clouds with two-level point processes. *Geoscience Remote Sens. IEEE Trans. On.* **53**, 1475–1489 (2015).
6. Leoncini, M. et al. Fully Integrated, 406 μA, 5/hr, full digital output Lissajous frequency-modulated gyroscope. *IEEE Trans. Industr. Electron.* **66**, 7386–7396 (2019).
7. Weiss, U. & Biber, P. Plant detection and mapping for agricultural robots using a 3D LIDAR sensor. *Rob. Auton. Syst.* **59**, 265–273 (2011).
8. Wong, J. K. W., Ge, J. & He, S. X. Digitisation in facilities management: a literature review and future research directions. *Autom. Constr.* **92**, 312–326 (2018).
9. Haleem, A. et al. Exploring the potential of 3D scanning in industry 4.0: an overview. *Int. J. Cogn. Comput. Eng.* **3**, 161–171 (2022).
10. Maneli, M. A. & Isafiade, O. E. 3D forensic crime scene Reconstruction Involving Immersive Technology: a systematic literature review. *IEEE Access.* **10**, 88821–88857 (2022).
11. Fu, J. et al. Recent Advancements in Augmented Reality for Robotic Applications: A Survey. Actuators vol. 12 Preprint at (2023). https://doi.org/10.3390/act12080323
12. Knopp, T. & Buzug, T. M. *Magnetic Particle Imaging: An Introduction to Imaging Principles and Scanner Instrumentation* (Springer, 2012).
13. Sehl, O. C., Gevaert, J. J., Melo, K. P., Knier, N. N. & Foster, P. J. A perspective on cell tracking with magnetic particle imaging. *Tomography* **6**, 315–324 (2020).
14. Han, X. et al. The applications of magnetic particle imaging: from cell to body. *Diagnostics* **10**, 1–12 (2020).
15. Yu, E. Y. et al. Magnetic particle imaging: a novel in vivo imaging platform for Cancer Detection. *Nano Lett.* **17**, 1648–1654 (2017).

16. Rivera-Rodriguez, A. et al. Tracking adoptive t cell immunotherapy using magnetic particle imaging. *Nanotheranostics* **5**, 431–444 (2021).
17. Tay, Z. W. et al. Magnetic particle imaging-guided heating in vivo using Gradient fields for arbitrary localization of magnetic hyperthermia therapy. *ACS Nano*. **12**, 3699–3713 (2018).
18. Buzug, T. M. & Borgert, J. Magnetic Particle Imaging: A Novel SPIO Nanoparticle Imaging Technique. vol. 115Springer Proceedings in Physics, (2007).
19. Panagiotopoulos, N. et al. Magnetic particle imaging: current developments and future directions. *Int. J. Nanomed.* **10**, 3097–3114 (2015).
20. Colombo, S., Lebedev, V., Tonyushkin, A., Pengue, S. & Weis, A. Imaging magnetic nanoparticle distributions by Atomic Magnetometry-based susceptometry. *IEEE Trans. Med. Imaging*. **39**, 922–933 (2020).
21. Borgert, J. et al. Fundamentals and applications of magnetic particle imaging. *J. Cardiovasc. Comput. Tomogr*. **6**, 149–153 (2012).
22. Elrefai, A. L., Sasayama, T., Yoshida, T. & Enpuku, K. AC Magnetization of Immobilized Magnetic Nanoparticles with different degrees of parallel alignment of Easy axes. *IEEE Trans. Magn.* **57**, 18–22 (2021).
23. Hadadian, Y., Uliana, J. H., Carneiro, A. A. O. & Pavan, T. Z. A Novel Theranostic platform: integration of Magnetomotive and Thermal Ultrasound Imaging with magnetic hyperthermia. *IEEE Trans. Biomed. Eng.* **68**, 68–77 (2021).
24. Top, C. B., Güngör, A., Ilbey, S. & Güven, H. E. Trajectory analysis for field free line magnetic particle imaging. *Med. Phys.* **46**, 1592–1607 (2019).
25. Reinhardt, S. C. M. et al. Ångström-resolution fluorescence microscopy. *Nature* **617**, 711–716 (2023).
26. Vogel, P. et al. Adjustable Hardware Lens for Traveling Wave Magnetic Particle Imaging. *IEEE Trans. Magn.* **56**, 1–6 (2020).
27. Bogner, W., Otazo, R. & Henning, A. Accelerated MR spectroscopic imaging—a review of current and emerging techniques. *NMR Biomed.* **34**, 1–32 (2021).
28. Werner, F., Gdaniec, N. & Knopp, T. First experimental comparison between the cartesian and the Lissajous trajectory for magnetic particle imaging. *Phys. Med. Biol.* **62**, 3407–3421 (2017).
29. Ozaslan, A. A., Alacaoglu, A., Demirel, O. B., Çukur, T. & Saritas, E. U. fully automated gridding reconstruction for non-cartesian x-space magnetic particle imaging. *Phys. Med. Biol.* **64**, 165018 (2019).
30. Tanguy, Q. A. A. et al. Real-time lissajous imaging with a low-voltage 2-axis MEMS scanner based on electrothermal actuation. *Opt. Express*. **28**, 8512 (2020).
31. Vogel, P. et al. Adjustable Hardware Lens for Traveling Wave Magnetic Particle Imaging. *IEEE Trans. Magn.* **56**, (2020).
32. Mukhatov, A., Le, T. A., Do, T. D. & Pham, T. T. Universal Behavior of the image resolution for different scanning trajectories. *Appl. Syst. Innov.* **6**, (2023).
33. Knopp, T. et al. Trajectory analysis for magnetic particle imaging. *Phys. Med. Biol.* **54**, 385–397 (2009).
34. Cabrera, G. F., Casassus, S. & Hitschfeld, N. Bayesian image Reconstruction based on Voronoi Diagrams. *Astrophys. J.* **672**, 1272–1285 (2008).
35. Wang, J., Zhang, G. & You, Z. Design rules for dense and rapid lissajous scanning. *Microsyst. Nanoeng.* **6**, 4–10 (2020).
36. Biederer, S. & Magnet-Partikel-Spektrometer *Entwicklung Eines Spektrometers Zur Analyse Superparamagnetischer Eisenoxid-Nanopartikel Für Magnetic-Particle-Imaging* (Springer-, 2012).
37. Zhang, P. et al. Dual-feature frequency Component Compression Method for accelerating Reconstruction in magnetic particle imaging. *IEEE Trans. Comput. Imaging*. **9**, 289–297 (2023).
38. Bazaei, A., Yong, Y. K. & Moheimani, S. O. R. High-speed lissajous-scan atomic force microscopy: scan pattern planning and control design issues. *Rev. Sci. Instrum.* **83**, 1–10 (2012).
39. Boiroux, D., Oke, Y., Miwakeichi, F. & Oku, Y. Pixel timing correction in time-lapsed calcium imaging using point scanning microscopy. *J. Neurosci. Methods*. **237**, 60–68 (2014).

Acknowledgements

This research was funded by the Science Committee of the Ministry of Science and Higher Education of the Republic of Kazakhstan with Grant no. AP22787355 and the Grant title: "Improving the Image Quality of Magnetic Particle Imaging by Optimizing the Scanning Paths".

Author contributions

Azamat Mukhatov prepared manuscripts, analyzed data, and ran simulations. In addition to securing funds, Ton Duc Do and Tri T. Pham developed, designed, and supervised the project. They also wrote codes, oversaw writing, review, and editing. Tuan-Anh Le contributed to the theory's formulation and the reconstruction of the image. Aizhan Tolebay prepared, reviewed, and edited the manuscript.

Declarations

Competing interests

The authors declare no competing interests.

Additional information

Correspondence and requests for materials should be addressed to T.D.D. or T.T.P.

Reprints and permissions information is available at www.nature.com/reprints.

Publisher's note Springer Nature remains neutral with regard to jurisdictional claims in published maps and institutional affiliations.

Open Access This article is licensed under a Creative Commons Attribution-NonCommercial-NoDerivatives 4.0 International License, which permits any non-commercial use, sharing, distribution and reproduction in any medium or format, as long as you give appropriate credit to the original author(s) and the source, provide a link to the Creative Commons licence, and indicate if you modified the licensed material. You do not have permission under this licence to share adapted material derived from this article or parts of it. The images or other third party material in this article are included in the article's Creative Commons licence, unless indicated otherwise in a credit line to the material. If material is not included in the article's Creative Commons licence and your intended use is not permitted by statutory regulation or exceeds the permitted use, you will need to obtain permission directly from the copyright holder. To view a copy of this licence, visit http://creativecommons.org/licenses/by-nc-nd/4.0/.

© The Author(s) 2025